RSC Advances

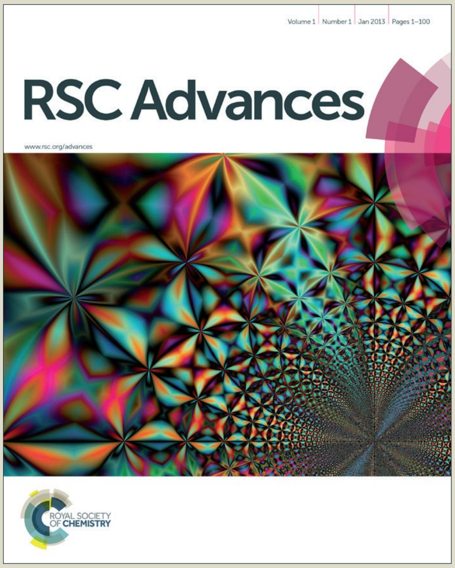

ROYAL SOCIETY
OF CHEMISTRY

www.rsc.org/advances

Graphene oxide aided structural tailoring of 3-D N-doped amorphous carbon network for enhanced energy storage

T.K. Shruthi, M. Saravana Kumar, Aswin Prathap, Naveen Chandrasekaran*

Electroplating Metal Finishing & Technology Division, CSIR - Central Electrochemical Research Institute, Karaikudi – 630 006, Tamil Nadu, India

***Corresponding Author's E-mail:** naveen@cecri.res.in, naveenumr@gmail.com

Abstract:

Organic aerogels are a class of materials most suited for their transformation into electrically conducting porous carbon networks. Typically, polymeric aerogels are prepared *via* base- or acid-catalyzed polymerization of organic monomers. In this work, we report the first synthesis of graphene oxide (GO) induced gelation of poly(urethane-amide) networks which upon pyrolysis yield monolithic N-doped amorphous carbon/reduced GO (rGO) aerogels. Here GO plays a significant multifunctional role of (i) inducing the gelation of poly(urethane-amide) networks; and (ii) tailoring the physical properties of N-doped amorphous carbon-rGO aerogels. The resulting aerogels were characterized by X-ray diffraction (XRD), N_2 sorption porosimetry, X-ray photoelectron spectroscopy (XPS), Fourier-Transform Infrared spectroscopy (FT-IR), Fourier-Transform Raman spectroscopy (FT-Raman), Field emission scanning electron microscopy (FE-SEM), High resolution transmission electron microscopy (HR-TEM) which supports the formation of highly porous carbon/rGO network. Importantly, the obtained N-doped amorphous carbon/rGO aerogels (0.76 wt% of GO) are electrically conducting with pore volume, pore diameter and surface area of 0.39 cm^3g^{-1} (69% mesopores), 36 nm and 260 m^2g^{-1} respectively. The significantly enhanced specific capacitance is derived from the tailored 3-D mesoporous structure of the N-doped amorphous carbon/rGO aerogels which consist of large pore volumes and predominant number of accessible mesopores allowing a low resistance path for inward and outward diffusion of electrolyte ions and endorsing high charge storage capability resulting in a superior specific capacitance of 260 F/g. The nanoporous networks in the as-prepared N-doped amorphous carbon/rGO serve as channels for quick ionic and electronic conduction. In addition to the enhanced physical properties achieved by addition of minimal amount of GO, the augmented specific capacitance can also be credited to the effective N-doping in ACGA-2 resulting in alteration of the electronic structure of rGO with increase in charge carrier density, and modification of interfacial and quantum capacitance.

Keywords: Organic aerogels, Graphene Oxide, Amorphous carbon, Reduced graphene oxide.

1. Introduction:

Ultra low-density three dimensional assemblies of inorganic or organic nanoparticles are referred to as aerogels [1,2]. Carbon aerogels are derived from pyrolysis of polymeric networks synthesized *via* sol-gel process ensued by supercritical drying wherein the solvent present in the wet gels is replaced with air [3-6]. The carbon networks thus formed are electrically conducting and have a clear three-dimensional porous network which permits efficient diffusion of ions. To date, various organic aerogels such as resorcinol-formaldehyde, melamine-formaldehyde, polyurethane, polyamide, polyimide and polybenzoxazine have been employed to prepare three dimensional carbon networks [7-11]. Interestingly, metal ion aided gelation of polymeric networks leads to new class of metal and carbide foams [12-14]. Technologies centered on carbon based materials have consolidated remarkable progress in the recent years. They exhibit diversity in physiochemical properties such as thermal and chemical stability, electrical conductivity and tunable morphologies which makes them potential candidates for a wide domain of applications such as energy storage, catalysis, sensing, and chromatography [15]. In due course, carbon aerogels are interesting materials as most of these applications demand high surface area, porosity and electrical conductivity. Graphene oxide obtained *via* oxidation of graphite contains oxygen functionalities (hydroxyl, epoxides and carboxylic acid) which upon thermal treatment yield two-dimensional reduced graphene oxide (rGO) sheets. Graphene, the wonder material is of researchers' attention due to its exceptional physico-chemical properties paving way for many technological applications [16, 17]. Rigorous attempts have been made to synthesize porous three- dimensional assemblies of rGO sheets to tap the exceptional properties of rGO and aerogels simultaneously [18-22]. For example, the carbon derived from resorcinol-formaldehyde has been used as interconnects to synthesize graphene aerogels [19, 20]. Meanwhile, reducing agents such as ascorbic acid have been employed in the formation of porous networks of rGO [21]. Graphene aerogels fabricated by these methods have been widely used as electrodes in supercapacitors which show moderate specific capacitance of 100-220 F/g which is normal for any graphene or carbon aerogel [21-26].

It is reasonable to envisage GO as catalyst for the gelation of polymeric networks keeping in mind the versatile functional groups that can readily react with diverse monomers [27, 28].

Nevertheless, there are a very few reports on GO induced gelation of polymeric or cellulose networks [29, 30]. For example, Zhang et al [30] reported graphene oxide induced gelation of cellulose networks with exceptional mechanical properties. Herein, we report the first GO induced gelation of poly(urethane-amide) (PUE) networks, by reacting the hydroxyl and carboxylic acid functional groups (present in GO) with tris(4-isocyanatophenyl)methane (TIPM), a tri-isocyanate. The pyrolyzed poly(urethane-amide)-GO (PUE-GO) networks resulted in N-doped amorphous carbon/rGO aerogels with enhanced specific capacitance relative to rGO and amorphous carbon aerogels reported earlier [21-26].The uniqueness of PUE networks can be traced to the rapid reaction of isocyanate and the nucleophiles present in TIPM and GO. Synthesis of N-doped amorphous carbon networks from the conventional melamine-formaldehyde and polybenzoxazine networks is a week long process, while mesoporous N-doped carbon networks derived from PUE networks can be prepared within two days. X-ray photo electron spectroscopy (XPS) reveal that the thermal decomposition of poly(urethane-amide) linkages lead to N-doping (pyridinic, pyrrolic and quarternary-N) into the carbon matrix.

2. Experimental Section:

2.1 Measurements.

X-ray diffraction measurements were performed using PANalytical instruments (Model No: PW3040/60 X'pert PRO, Cu K_α radiation, λ = 1.5414 Å) at a scan rate and step size of $1.2^o min^{-1}$ and 0.02^o sec^{-1} respectively. Analysis of the XRD patterns was done using Hi Score search match software and X'Pert Plus crystallographic analysis software with Rietveld capability. X-ray photo electron spectroscopy was performed using SPECS, Phoibos 100 MCD Analyzer with pass energy of 20 eV (Al Kα anode (1486.6eV)) in ultrahigh vacuum (5×10-10mbar). Raman spectroscopy was carried out using a Renishaw Ramanscope 2000 spectrometer with HeNe 632 nm laser. Morphological characterizations were done using Field Emission Scanning Electron Microscope (Zeiss supra 55VP) High resolution-Transmission Electron Microscope images (HR-TEM) for the samples were taken using Tecnai G2 (FEI make). To retain the volume of the gel intact, supercritical drying was carried out in a critical point drier (Model No: E3100, Quorum Technologies, Ltd) using CO_2 at critical pressure and temperature of 1200 psi and 31.2 ^oC respectively. Infrared spectra were obtained on a Bruker Tensor 27 FT-IR Spectrometer using KBr pellets. The samples were pyrolyzed in a tube furnace at 800 ^{o}C at 5 ^{o}C min^{-1}for 5 h under flowing Ar at a flow rate of 120 mL min^{-1}. N_2 sorption isotherms were obtained using Quadrasorb Four Station Surface Area. The bulk densities (ρ_b) were calculated using the physical dimensions and mass of the samples using the formula (ρ_b = mass/(π*r^2*h) (where, r and h is the radius and height of the samples).Skeletal densities (ρ_s) were determined by Helium pycnometry (Micromeritics (AccuPyc 1330) instruments). The porosity values (Π) of the aerogels were determined from the bulk and skeletal density values according to equation, $\Pi = 100 \times [(1/\rho_s) - (1/\rho_b)]/ (1/\rho_s)$ [6-10].

2.1.a Materials.

Graphite powder (300 mesh, 99%) was obtained from Alfa Aesar. Sodium nitrate ($NaNO_3$), Conc.H_2SO_4 (98%), $KMnO_4$ and 30% H_2O_2 were used as received form Sigma-Aldrich. N, N'-Dimethyl formamide (DMF) (99.96%) was purchased from TCI Chemicals. Desmodur RE (tris(4-isocyanatophenyl)methane) (TIPM) (~27% in ethyl acetate) was purchased from Bayer-India.

2.2. Electrochemical Characterization.

Cyclic voltammetry measurements were carried out in a conventional three-electrode cell at 25 °C, with the electrode made by coating the active materials on a Pt substrate (1 x 1cm^2) as the working electrode, Pt foil (2 cm^2)as the counter electrode and saturated calomel electrode as the reference electrode. The measurements were carried out in 1 M H_2SO_4 as electrolyte. All the electrochemical experiments were carried out using an electrochemical workstation (Autolab PGSTAT 302N). Electrodes for the capacitance measurements were prepared by coating the active materials on the Pt substrate. The slurry was prepared using 90% of active material and 10% PTFE binder in DMF under ultrasonication. An appropriate quantity of the slurry was coated on a pre-washed Pt substrate by drop casting and then dried at 120°C in a vacuum oven. The material loading was maintained at 2 mg cm^{-2}. The specific capacitance was calculated from the discharge curve using the equation: $C=I*\Delta t/ (m*\Delta V)$, where I (A),$\Delta t$ (s), m (g) and ΔV (V) are the discharge current, discharge time from the charge-discharge curve, mass of the active material employed and potential difference respectively.

2.3. Preparation of Graphene Oxide.

Graphene oxide was prepared by modified Hummer's method [31]. Typical synthetic procedure of GO includes slow addition of 100 mL of concentrated H_2SO_4 to a mixture of 3 g of graphite powder and 3 g of $NaNO_3$ in a round bottomed flask; the temperature being maintained at 0^oC using an ice bath under constant stirring. To the obtained black mixture, 12 g of $KMnO_4$ was added slowly with vigorous stirring. After the complete addition of $KMnO_4$, the mixture was maintained at 0^oC under vigorous stirring. The temperature of the bath was increased and maintained at 35 ^oC for 72 h. The brownish precipitate, obtained after this step was washed with distilled water then the temperature was raised to 90 ^oC. The solution obtained was diluted with 250 mL of distilled water. The diluted solution was kept standstill for 48 h before the addition of 10 mL of 30% H_2O_2.The rGO oxide obtained was brown in colour and was washed with 4% HCl followed by several washes with distilled water to ensure that GO does not contain any traces of acid impurities. After several washings, barium sulphate was added to the filtrate to ensure there is no precipitate formation, which may be an indication of HCl free GO. Finally the GO was dried under vacuum filtration.

2.3.a. Preparation of N-doped Amorphous Carbon-rGO aerogels (ACGA).

The typical synthetic procedure for ACGA is given in scheme 1 and includes, ultrasonicating 2 mg (0.72 wt%)and 10 mg (3.6 wt%)of GO in 10 mL DMF for 2 h to get a stable dispersion. To the obtained stable dispersion of rGO oxide, 0.275 g (0.074 M) of Desmodur RE (tris(4-isocyanatophenyl)methane) (TIPM) was added. The resulting sol was poured in polypropylene molds. The gelation time of the poly (urethane-amide)-rGO oxide (PUE-GO) gels was found to be ~30 min and 12 min for 0.72 and 3.6 wt% respectively. In the absence of GO, the gelation takes ~6h.The PUE-GO gels were washed with DMF (3 × 8 h) followed by subsequent acetone (3 × 8 h) washes. The wet gels were dried in an autoclave using $scCO_2$. All samples showed minimal shrinkage of ~10-12 % upon solvent exchange and supercritical drying.The PUE-GO gels were pyrolyzed under Ar at 800 ^oC to obtain N-doped amorphous carbon/rGO aerogels (ACGA).The pyrolyzed PUE-GO aerogel samples with 0.72, 3.6 wt% and without GO are denoted as ACGA-2 and ACGA-10 and ACA respectively.

3. Results and Discussion:

3.1. Gelation mechanism of PUE-GO gels:

The gelation of PUE-GO gels takes place *via* scheme 1 where the GO functionalities such as hydroxyl groups at the basal plane and carboxylic acid groups at the edges react with isocyanate to yield urethane and amide respectively. The gelation time can be controlled by varying the concentrations of GO and TIPM. FTIR spectra of as- prepared GO as shown in Figure 1 displays a characteristic C=O peak at 1708 cm^{-1}, OH deformation vibration at 1370 cm^{-1}, C-OH stretching vibration at 1224 cm^{-1}, C-O vibration at 1037 cm^{-1} and broad intense OH peak at 3400 cm^{-1}[24]. The disappearance of the isocyanate peak at 2265 cm^{-1}and formation of peaks in PUE-GO gels such as the NH stretch at 3313 cm^{-1}, amide carbonyl stretching at 1654 cm^{-1}, new peaks at 1509 cm^{-1} correspond to the NH bending vibration coupled with the C–N stretch confirm the reaction between GO and isocyanate yielding PUE-GO gels with covalent amide and urethane linkages.

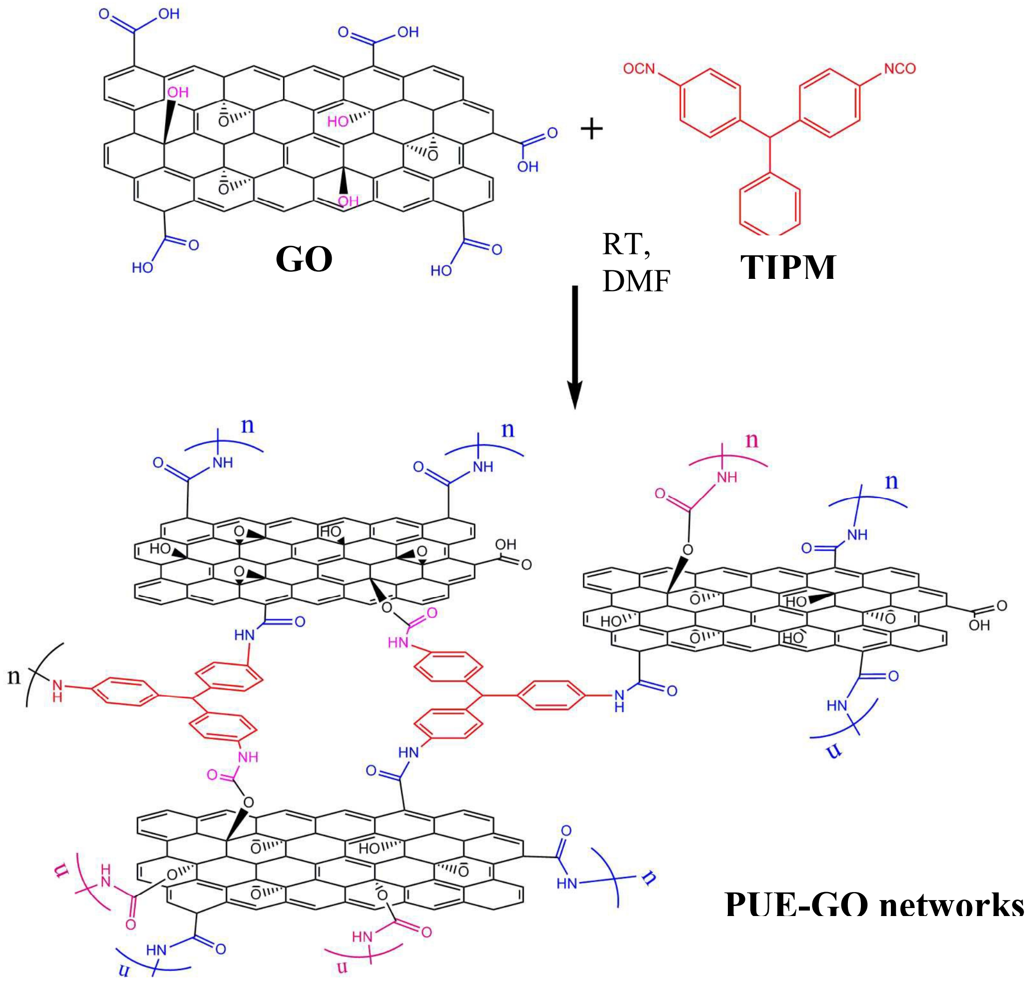

Scheme 1: Proposed mechanism for formation of PUE-GO networks

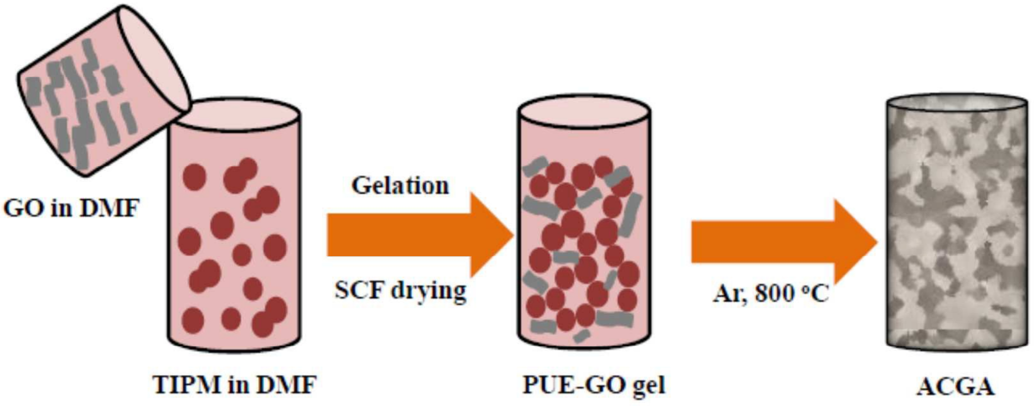

Scheme 2: Synthetic scheme of ACGA

3.2. Synthesis and Characterization of ACGA:

The *as prepared* PUE-GO gels were pyrolyzed in a tubular furnace under Ar at 800 °C at a heating rate of 5°C/minute as shown in scheme 2. The obtained N-doped amorphous carbon/rGO aerogels were found to be monolithic. Physical properties of GO, ACA, ACGA-2 and ACGA-10 are summarized in Table 1. Bulk densities of ACA, ACGA-2 and ACGA-10 were found to increase upon addition of GO ranging from 0.17 to 1.21 g/cc. Skeletal density for all three samples is in the range of 1.88-1.93 g/cc. Skeletal density of GO was determined to be 1.92 g/cc and is in close agreement with the reported value [32].The porosity values calculated from the difference between the reciprocals of bulk and skeletal densities of ACA, ACGA-2 and ACGA-10 indicate a decrease in the void space upon addition of GO. The drastic increase in the bulk density and subsequent decrease in porosity can be ascribed to the increase in the concentration of GO resulting in pore clogging.

Table 1: Selected physical properties of GO, ACA, ACGA-2 and ACGA-10 samples

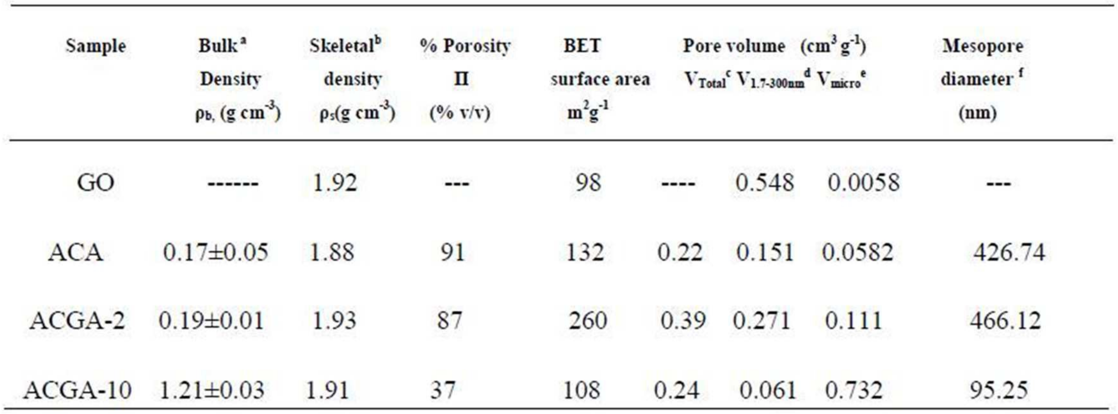

Sample	Bulk[a] Density ρ_b, (g cm^{-3})	Skeletal[b] density ρ_s(g cm^{-3})	% Porosity Π (% v/v)	BET surface area m^{2}g^{-1}	Pore volume (cm^3 g^{-1}) V_{Total}[c]	$V_{1.7\text{-}300nm}$[d]	V_{micro}[e]	Mesopore diameter[f] (nm)
GO	------	1.92	---	98	----	0.548	0.0058	---
ACA	0.17±0.05	1.88	91	132	0.22	0.151	0.0582	426.74
ACGA-2	0.19±0.01	1.93	87	260	0.39	0.271	0.111	466.12
ACGA-10	1.21±0.03	1.91	37	108	0.24	0.061	0.732	95.25

[a]Average of 5 samples (Mold Diameter = 1 cm), [b] Average of 50 measurements of a sample , [c] BJH desorption cumulative pore volume < 884 nm, [d] BJH desorption pore volume between 1.7-300 nm, Cumulative pore volume of N_2 adsorbed at $P/Po \leq 0.1$, [f] Maxima of BJH desorption plots,

Figure 2(a-d) displays FE-SEM images of GO, ACA, ACGA-2 and ACGA-10. Microscopically, GO was found to be in the form of wrinkled sheets. FE-SEM images of ACA derived from PUE aerogels were found to have an interconnected meso- and macro-porous 3-D structure. The images of ACGA-2 show interconnected sheet like structure with voids in the mesoporous regime (< 50 nm). However, FESEM images of ACGA-10 with a higher loading of GO (10 wt%) show no pores, consistent with the observation of reduced porosity and high density values (Table 1) which could be due to the stacking of rGO layers leading to pore clogging. Figure 3 displays the HR-TEM images of GO, ACA, ACGA-2 and ACGA-10 samples. Figure 3a exhibits the TEM image of GO with few stacked sheets. Despite the harsh oxidation steps, the GO sheets was found to maintain its long range orientational order which is evident from the corresponding Selected Area Diffraction Pattern (SAED) of GO. The SAED pattern of GO reveals the disoriented hexagonal patterns with fuzzy rings which can be corroborated to the presence of oxygen functionalities [33]. Figure 3b displays the TEM image of ACA with interconnected sheets in the range of 50-100 nm. The corresponding SAED pattern of ACA shows diffuse rings which is typical of amorphous carbon. Figure 3c reveals the TEM image of ACGA-2 with interconnected sheets similar to ACA with sheet size in the range of 20-100 nm. It is evident from TEM images of ACGA-2 that the interconnected amorphous carbon sheets leaves voids in the mesopore regime (~20 nm). Owing to the minimal addition of GO and look-alike morphology of amorphous carbon and rGO, it was difficult to distinguish the presence of amorphous carbon and rGO in the ACGA-2 sample. However, the SAED pattern of the corresponding sample reveals bright spots and diffused rings which can be ascribed to the presence of rGO and amorphous carbon respectively. Figure 3d shows the TEM image of ACGA-10, with rGO layers masking the amorphous carbon matrix. Similar to ACGA-2 the SAED pattern of ACGA-10 sample showcased bright spots and diffuse rings pertaining to the presence of both rGO and amorphous carbon respectively.

Textural characteristics of GO, AC, ACGA-2 and ACGA-10 were investigated by N_2 sorption measurements. N_2 sorption isotherm of GO in Figure 4a appears to be of type IV with H_2 hysteresis loop from 0.3 to 0.98 relative pressure and with a BET surface area of 98 m^2/g. The adsorption isotherm of GO shows both meso-and microporosity which may be attributed to the inter-layer voids between the GO sheets and due to defects in the sheets [34]. The N_2 sorption isotherms of ACA and ACGA-2 (Figures 4(b and c), rise above a relative pressure of 0.9 and do not attain saturation. They also indicate narrow hysteresis loops and considerable specific volumes adsorbed at low relative pressures indicating the presence of both meso-and macro-pores. It is worthy to note that despite the presence of large number of mesopores in ACA (68%), the total pore volume (V_T) for ACA (0.22 cm^3/g) is much less as compared to ACGA-2 (0.39

cm^3/g). The presence of large number of mesopores (69%) and large pore volume may have resulted in the double fold increase in surface area leading to a higher charge storage capability in ACGA-2. On the contrary, N_2 sorption isotherm of ACGA-10 shown in Figure 4d follows a typical type II isotherm that can be ascribed to non-porous materials, but the hysteresis at low relative pressures is indicative of the presence of micropores. Therefore, ACGA-10 consists of both micropores (30.5%) and macropores (44.5%). The presence of micropores may have resulted in the observed surface area of 108 m^2/g. Low pressure hysteresis observed for ACA and ACGA-10 samples can be attributed to the presence of narrow pores exhibiting the presence of a potential barrier for inward and outward diffusion. Pore volume and surface area determined from N_2 sorption isotherms were found to be maximum when the concentration of GO was minimum.

Figure 5 compares the X-ray diffraction patterns of graphite, GO, ACA, ACGA-2 and ACGA-10. The diffraction pattern of GO suggests complete exfoliation of graphite by the disappearance of the characteristic peak of graphite at ~26^o and formation of a new reflection at ~11.6^o [24]. An increase in the interlayer spacing of graphite from 0.34 to 0.83 nm also confirms formation of GO. The ACA sample was found to be amorphous with a characteristic broad reflection at ~$26^o$and an interlayer spacing of ~0.36 nm. The interlayer spacing values for ACGA-2 and ACGA-10 were found to be similar (~0.36 nm) suggesting that there is no intercalation of rGO between amorphous carbon. This is well supported by the HR-TEM image of ACGA-10 which evidently reveals the masking of the amorphous carbon surface by rGO.

The successful incorporation of rGO in the amorphous carbon matrix was determined by Raman spectroscopy. Comparison of Raman spectra of GO, ACA and ACGA-2 and ACGA-10 is shown in Figure 6. Two prominent peaks at ~ 1350 cm^{-1} and ~1580 cm^{-1} correspond to D and G band respectively. The D band arises from the structural defects whereas the G band corresponds to the first-order scattering of the E_{2g} mode from the sp^2 domains [35].The gradual increase in I_D/I_G for ACGA-2 and ACGA-10 after addition of GO relative to ACA indicates an increase in defective sites due to the incorporation of the heteroatom [36].

XPS was used to determine the % content and types of nitrogen species present in the aerogel samples. Table 2 shows the elemental composition of GO, ACA, ACGA-2 and ACGA-10 samples quantified from XPS. As-prepared GO displayed high oxygen content (43.44%) with absence of nitrogen species. Upon pyrolysis at elevated temperature, ACA, ACGA-2 and

ACGA-10 samples show carbon content as high as 89.6, 84.07 and 84.82% respectively. The drastic increase in carbon content can be attributed to the successful reduction of oxygen functionalities upon pyrolysis at elevated temperatures. The % atomic nitrogen present in ACA, ACGA-2 and ACGA-10 samples were found to be 2.12, 4.67 and 4.72 respectively. The nitrogen atoms doped into the amorphous carbon/rGO matrix can be ascribed to the decomposition of poly(urethane-amide) linkages upon thermal treatment [37-39].As observed from Table 2,the N content increases from ACA to ACGA-10. This observation is due to the fact that N-doping occurs only in the amorphous carbon matrix of ACA while N-doping in ACGA occurs both in the rGO layers as well as in the amorphous carbon matrix.

Table 2. Elemental composition of GO, ACA, ACGA-2 and ACGA-10 by XPS

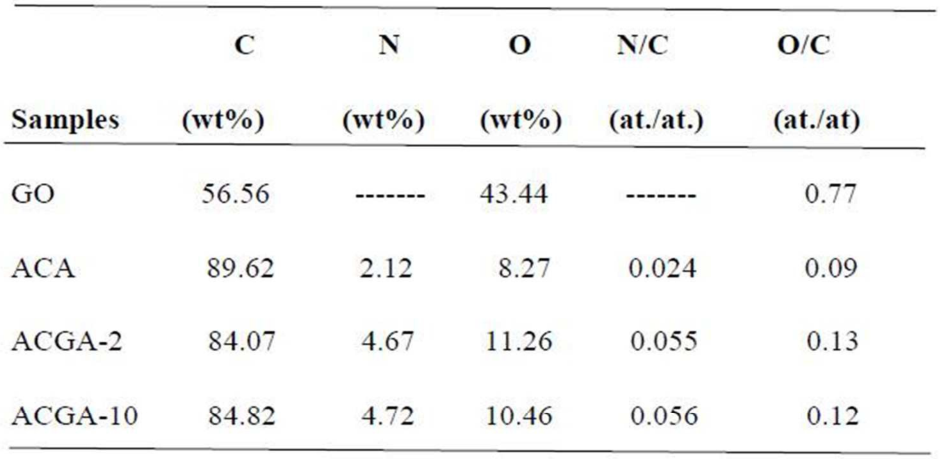

Samples	C (wt%)	N (wt%)	O (wt%)	N/C (at./at.)	O/C (at./at)
GO	56.56	-------	43.44	-------	0.77
ACA	89.62	2.12	8.27	0.024	0.09
ACGA-2	84.07	4.67	11.26	0.055	0.13
ACGA-10	84.82	4.72	10.46	0.056	0.12

XPS spectra shown in Figure 7a, reveals that the as prepared GO possesses no N peak. Analysis of the C1s spectrum of GO shown in Figure 7b, indicates the presence of oxygen functionalities with their signature peaks at higher binding energies corresponding to C-C, C-O, C=O, O=C-OH at 284.86 eV, 285.8 eV, 287.2 eV and 288.6 eV respectively [24]. XPS spectra of ACA, ACGA-2 and ACGA-10 shown in Figure 7c, display intense C-C peak at 284.86 eV, small signals at higher binding energies correspond to C=N and C-N. The deconvoluted high resolution spectra of N 1s peak of all three samples shown in Figure 7d indicates the presence of three peaks at binding energies 393.8, 400.1 and 400.95 eV corresponding to pyridinic, pyrrolic and quaternary nitrogen, respectively [26, 40]. From the physical and chemical characterization of PUE-GO and ACGA, it is evident that GO plays a vital role in (i) inducing the gelation of poly(urethane-amide) networks; and (ii) tailoring the physical properties of N-doped amorphous carbon-rGO aerogels.

3.3 Electrochemical investigation of ACGA:

Investigations for the suitability of ACGA as supercapacitor electrode materials were carried out in a standard three electrode system using 1M H_2SO_4 electrolyte. It can be seen form Figure 8a that all the cyclic voltammograms are nearly rectangular in shape indicating pure electrical double layer capacitance, consistent with the behavior of conventional carbon aerogels. The near-linear charge/discharge curves also endorse the double layer capacitive behavior of ACA, ACGA-2 and ACGA-10. At a current density of 0.5A/g, the specific capacitance of ACGA-2 as calculated from the slope of the charge discharge curves (Figure 8b) was found to be 260F/g which is higher than the specific capacitance values of ACA (31 F/g) and ACGA-10 (9 F/g) at the same current density. The obtained specific capacitance value for ACGA-2 is much higher when compared to 3-D nitrogen and boron doped graphene networks (128, 240 F/g) [41], hydrogels (160, 166, 186, 190 F g^{-1}) [42-46] and carbon nanotube spaced (245 F/g) [47] electrodes in aqueous medium. Nevertheless, there are few reports with better specific capacitance for graphene aerogels alone [48, 49]. Although the surface area of ACGA-2 is not very high as compared to other rGO/carbon based electrode materials, the presence of accessible mesopores promotes shorter diffusion pathways with less resistance for the electrolyte ions thereby increasing charge storage at these sites. Its large pore volume allows efficient double layer formation and dynamic charge propogation thus efficiently utilizing the electrochemically active electrode surface. Despite the presence of mesopores (25%), the extremely low capacitance exhibited by ACGA-10 may be realized from the narrow pore width (~9 nm) which is in close proximity to the micropore range. Additionally, the augmented specific capacitance can be credited to the effective N-doping in ACGA-2 resulting in alteration of the electronic structure of rGO with increase in charge carrier density, and modification of interfacial and quantum capacitance. Although the N-content of ACGA-10 is similar to ACGA-2, the same effect is not observed in ACGA-10 sample because of the disordered stacking of rGO layers on the surface of the amorphous carbon thereby clogging pores and hampering inward and outward diffusion of electrolyte ions, as evident from HR-TEM image of ACGA-10 [50]. Figure 8c shows the variation of current density for ACGA-2 as a function of potential sweep rate. It can be observed that even at high scan rates, the shape of the CV remains rectangular with slight deviations at higher potentials owing to the insufficient time available for charge propagation during quick scans.

Figure 8d displays the rate performance of ACGA-2 determined by galvanostatic charge/discharge at increasing current densities. It is observed that the specific capacitance of the aerogel decreases with increasing current density. On increasing the current density from 0.5 to 5A/g, the capacitance value for ACGA-2 decreases to 188F/g and a further decrease to 175F/g was observed at a current density of 10A/g. Although there is a slight deterioration in the capacitance value, the curves exhibit symmetry and linearity affirming the stability of ACGA-2 at high current densities which is due to the excellent ionic and electronic transport within the porous network. A long cycle life is a vital requirement for an electrode material when considered for supercapacitor applications. The electrochemical cycling stability of ACGA-2 was evaluated by repeated charge-discharge cycles between the potential window of -0.2V to 0.8V at a current density of 0.5A/g (Figure 8e). Even after 2000 continuous cycles, only a 3% decay in specific capacitance was observed for ACGA-2 which is indicative of the excellent rate performance of ACGA due to the robust cross-links, hierarchical mesoporous structure and enhanced surface area of ACGA-2 relative to ACA and ACGA-10.

The electrochemical impedance measurements were conducted for ACA, ACGA-2 and ACGA-10 samples in the frequency range of 1 MHz to 100 mHz at an open circuit potential and amplitude of 0.34 V and 5 mV respectively and the resulting Nyquist plots are shown in Figure 9. The presence of a distinctive semicircle in the high frequency region of a Nyquist plot denotes the charge transfer resistance of a sample. The faster kinetics of electrolyte ions can be interpreted from the radius of this semicircle, generally smaller the radius of the semicircle, lesser is the charge transfer resistance (R_{ct}) [49, 50]. The presence of an indistinct semicircle for ACGA-2 relative to ACA and ACGA-10 in the high frequency region is indicative of a very low charge transfer resistance at the electrode/electrolyte interface favoring faster ion transfer kinetics. The low R_{ct} for ACGA-2 suggests high conductivity which may be due to its well-connected porous carbon network with higher pore volume and surface area providing electrolyte ions the liberty to permeate easily into the mesopores of the electrode material. The equivalent series resistance (ESR) calculated from the x-intercept of the Nyquist plot shows that ACGA-2

(0.8 ohm) has the least ESR compared to ACGA-10 (1.9 ohm) and ACA (1.72 ohm). This result is consistent with our claim that a higher loading of GO results in precluding the active surface area of the electrode material. The slope of the 45 degree portion of the curve is called the Warburg impedance and is indicative of the ion diffusion at the electrode/electrolyte interface. The short Warburg line for ACGA-2 connotes a short ion diffusion path which allows a low resistance path for ion penetration and an easy access to the surface area. As seen from Figure 8, the near vertical line at lower frequency region for ACGA 2 is an indication of pure capacitive behaviour. The slanting lines observed for ACA and ACGA-10 can be attributed to the limited diffusion of electrolyte ions owing to the presence of narrow pores resulting in lower charge storage.

4. Conclusions:

In summary, we have demonstrated GO induced gelation of PUE gels:1. The gelation time of PUE-GO gels can be controlled by varying the concentration of GO. 2. The pyrolyzed PUE-GO gels under inert atmosphere yield ACGA with enhanced surface area and porosity. Interestingly, ACGA-2 with a minimum concentration of GO (0.72 wt%) was found to be mesoporous with a surface area of 260 m^2/g. The as-prepared ACGA-10 gels were found to contain narrow pores and the clogging of pores due to stacking of rGO resulted in decreased surface area and porosity (as evident from N_2 sorption isotherms and microscopic images). The decomposition of polyurethane and amide linkages resulted in N-doping into the carbon matrix. The rapid reaction of isocyanate and the nucleophiles in GO results in faster gelation of PUE networks in turn assisting in time efficient synthesis of N-doped amorphous carbon aerogels. Electrochemical investigations suggest that ACGA-2 sample displays a specific capacitance of 260 F/g, a value considered high for rGO and amorphous carbon aerogels. Furthermore, the material displayed a high electrochemical cycling stability with a capacitance decay of only 3% after 2000 cycles. The enhanced specific capacitance of ACGA-2 is due to the tailoring of the porous structure by GO resulting in a hierarchical predominantly mesoporous network offering efficient ionic transport and low resistance diffusion pathways. The enhanced capacitance of ACGA-2 can be credited to the structural modification of amorphous carbon matrix brought about by the addition of minimal amount of GO and also by the modification of electronic structure accompanied by increased charge carrier density which in turn enhances the interfacial capacitance between the electrode material and the electrolyte. Also, it has to be clarified that the structural modification of amorphous carbon matrix achieved by minimal addition of GO has to be further explored. This 3-D porous structured network can also be extended to other device applications such as Li-ion batteries, hybrid supercapacitors etc.

Acknowledgements:

Authors acknowledge CSIR for 12th five year project (Project No: CSC 0114) and Department of Science and Technology for funding (GAP 10/14) under fast track scheme.

References:

1. R. W. Pekala, *J. Mater. Sci.*, 1989, **24**, 3221-3227.
   A. C. Pierre and G. M. Pajonk, *Chem. Rev*., 2002, **102**, 4243-4265.
2. S. A. Al-Muhtaseb and J. A. Ritter, *Adv. Mater*, 2003, **15**, 101-114.
3. T. Yamamoto, T. Sugimoto, T. Suzuki, S. R. Mukai, H. Tamon, *Carbon*, 2002, **40**, 1345-1351.
4. K. Chan, J. Ding, J. Ren, S. Cheng, K. J. Tsang, *J. Mater. Chem*, 2004, **14**, 505-516.
5. S. Mulik, C. S. Leventis, N. Leventis, Chem. Mater, 2008, **20**, 6985-6997.
6. N. Leventis, C. S. Leventis, N. Chandrasekaran, S. Mulik, Z. J. Larimore, H. Lu, G. Churu, J. T. Mang, *Chem. Mater*, 2010, **22**, 6692-6710.
7. C. Chidambareswarapattar, Z. Larimore, C. S. Leventis, J. T. Mang, N. Leventis, *J. Mater. Chem*, 2010, **20**, 9666-9678.
8. N. Leventis, C. S. Leventis, N. Chandrasekaran, S. Mulik, C. Chidambareswarapattar, A. Sadekar, D. Mohite, S. Mahadik, Z. J. Larimore, H. Lu, G. Churu, J. Mang, MRS Proceedings, 2011, **1306,** mrsf10-1306-bb03-0.
9. C. Chidambareswarapattar, L. Xu, C. S. Leventis, N. Leventis, *RSC. Adv*, **3**, 26459-26469.
10. M. Perez-Cadenas, C. Moreno-Castilla, F. Carrasco-Marin, A. F. Perez-Cadenas, *Langmuir*, 2009, **25**, 466-470.
11. N. Leventis, N. Chandrasekaran, C. S. Leventis, A. Mumtaz, *J. Mater. Chem*, 2009, **19**, 63-65.

12. N. Leventis, N. Chandrasekaran, A. G. Sadekar, S. Mulik, C. S. Leventis, *J. Mater. Chem*, 2010, **20**, 7456-7471.
13. S. Mahadik-Khanolkar, S. Donthula, C. S. Leventis, N. Leventis, *Chem. Mater*, 2014, **26**, 1303-1317.

14. T. N. Kumar, S. Sivabalan, N. Chandrasekaran, K. L. N. Phani, *Chem. Commun*, 2015, **51**, 1922-1925.
    A. K. Geim, K. S. Noveslov, *Nat. Mater*, 2007, **6**, 183-191.
15. V. Chabot, D. Higgins, A. Yu, A. Xiao, Z. Chen, J. Zhang, Energy Environ. Sci. 2014, **7**, 1564-1596.
16. M. A. Worsley, P. J. Pauzauskie, T. Y. Olson, J. Biener, J. H. Satcher, T. F. Baumann, *J. Am. Chem. Soc*, 2010, **132**, 14067-14069.
17. M. A. Worsley, S. O. Kucheyev, H. E. Mason, M. D. Merrill, B. P. Meyer, J. Lewicki, M. E. Suss, M. Stadermann, P. J. Pauzauskie, J. H. Satcher, J. Biener, T. F. Baumann, *Chem. Commun*, 2012, **48,** 8428-8430.
18. X. Zhang, Z. Sui, B. Xu, S. Yue, Y. Luo, W. Zhan, B. Liu, J. *Mater. Chem*, 2011, **21**, 6494-6497.
19. D. Zhang, X. Wen, L. Shi, T. Yan, J. Zhang, *Nanoscale*, 2012, **4**, 5440-5446.
20. H. Li, L. Pan, C. Nie, Y. Liu, Z. Sun, *J. Mater. Chem*, 2012, **22**, 15556-15561.
21. K. Gao, Z. Shao, J. Li, X. Wang, X. Peng, W. Wang, F. Wang, *J. Mater. Chem. A*, 2013, **1**, 63-67.
22. E. Wilson, M. F. Islam, *ACS Appl. Mater. Interfaces*, 2015, **7**, 5612-5618.
23. Z-Y. Sui, Y-N. Meng, P-W. Xiao, Z-Q. Zhao, Z-X. Wei, B-H. Han, *ACS Appl. Mater. Interfaces*, 2015, **7**, 1431-1438.
24. D. R. Dreyer, S. Park, C. W. Bielawski, R. S. Ruoff, *Chem. Soc. Rev*, 2010, **39**, 228-240.
25. H. Bai, C. Li, X. Wang, G. Shi, *J. Phys. Chem. C*, 2011, **115**, 5545-5551.
26. M. Li, J. Ding, J. Xue, *J. Mater. Chem. A*, 2013, **1**, 7469-7476.
27. U. N. Maiti, J. Lim, K. E. Lee, W. J. Lee, S. O. Kim, *Adv. Mater*, 2014, **26**, 505.
28. J. Zhang, Y. Cao, J. Feng, P. Wu, *J. Phys. Chem. C*, 2012, **116**, 8063-8068.
29. W. Ouyang, J. Sun, J. Memon, C. Wang, J. Geng, Y. Huang, *Carbon*, 2013, **62**, 501-509.
30. Y. Zhang, W. Fan, Y. Huang, C. Zhang, T. Liu, *RSC. Adv*, 2015, **5**, 1301-1308.

31. W. S. Hummers Jr., R. E. Offeman, J. Am. Chem. Soc. 1958, **80**, 1339.
32. M. S. L. Hudson, H. Raghubanshi, S. Awasthi, T. Sadasivam, A. Bhatnager, S. Simizu, S. G. Sankar, O. N. Srivatsava, *Int. J. Hydrogen Energ*, 2014, **39**, 8311-8320.
33. N. R. Wilson, P. A. Pandey, R. Beanland, R. J. Young, I. A. Kinloch, L. Gong, Z. Liu, K. Suenga, J. P. Rourke, S. J. York, J. Sloan, *ACS Nano*, 2009, **3**, 2547-2556.
34. B. Xu, S. Yue, Z. Sui, X. Zhang, S. Hou, G. Cao, Y. Yang, Energy Environ. Sci, 2011, **4**, 2826-2830.
35. M. A. Worsley, T. Y. Olson, J. R. I. Lee, T. M. Willey, M. H. Nielsen, S. K. Roberts, P. J. Pausauzike, J. Biener, J. H. Satcher, T. F. Baumann, *J. Phys. Chem. Lett*, 2011, **2**, 921-925.
36. L. Qu, Y. Liu, J-B. Beak, L. Dai, ACS Nano, 2010, **4**, 1321-1326.
37. Z. Lin, G. Waller, Y. Liu, M. Liu, C-P, Wong, *Adv. Energy. Mater*, 2012, **7**, 884-888.
38. L. Sun, L. Wang, C. Tan, T. Tan, Y. Xie, K. Shi, M. Li, H. Fu, *RSC. Adv*, 2012, **2**, 4498-4506.
39. H-L. Guo, P. Su, X. Kang, S-K, Ning, *J. Mater. Chem. A*, 2013, **1**, 2248-2255.
40. D. Long, W. Li, L. Ling, J. Miyawaki, I. Mochida, S-H. Yoon, *Langmuir*, 2010, **26**, 16096-16102.
41. Z. S. Wu, A. Winter, L. Chen, Y. Sun, A. Turchanin, X. Feng, K. Mullen, *Adv. Mater*, 2012, **24**, 5130-5135.
42. Y.X. Xu, K.X. Sheng, C. Li, G.Q. Shi, *ACS Nano*, 2010, **4**, 4324-4330.
43. P. Chen, J. J. Yang, S. S. Li, Z. Wang, T. Y. Xiao, Y. H. Qian, S. H. Yu, *Nano Energy*, 2013, **2**, 249-256.
44. Y. Xu, Z. Lin, X. Huang, Y. Liu, Y. Huang, X. Duan, *ACS Nano*, 2013, **7**, 4042-4049.
45. W. Chen, L. Yan, *Nanoscale*, 2011, **3**, 3132-3137.
46. L. Zhang, F. Zhang, X. Yang, G. Long, Y. Wu, T. Zhang, K. Leng, Y. Huang, Y. Ma, A. Yu, Y. Chen, Sci. Rep, 2013, **3**, 1408-1416.
47. Q. Shao, J. Tang, Y. Lin, J. Li, F. Qin, J. Yuan, L-C. Qin, *J. Power Sources*, 2015, **278**, 751-759.
48. S. Ye, J. Feng, P. Wu, *ACS Appl. Mater. Interfaces*, 2013, **5**, 7122–7129.

49. S. H. Aboutalebi, R. Jalili, D. Esrafilzadeh, M. Salari, Z. Ghaolamvand, S. A. Yamini, K. Konstantinov, R. L. Sheperd, J. Chen, S. E. Moulton, P. C. Innis, A. I. Minett, J. M. Razal, G. C. Wallace, *ACS Nano*, 2014, **8**, 2456–2466.
50. H. M. Jeong, J. W. Lee, W. H. Shin, Y. J. Choi, H. J. Shin, Y. J. Choi, J. K. Kang, J. W. Choi, Nano Letters, 2011, **11**, 2472-2477.

Figures:

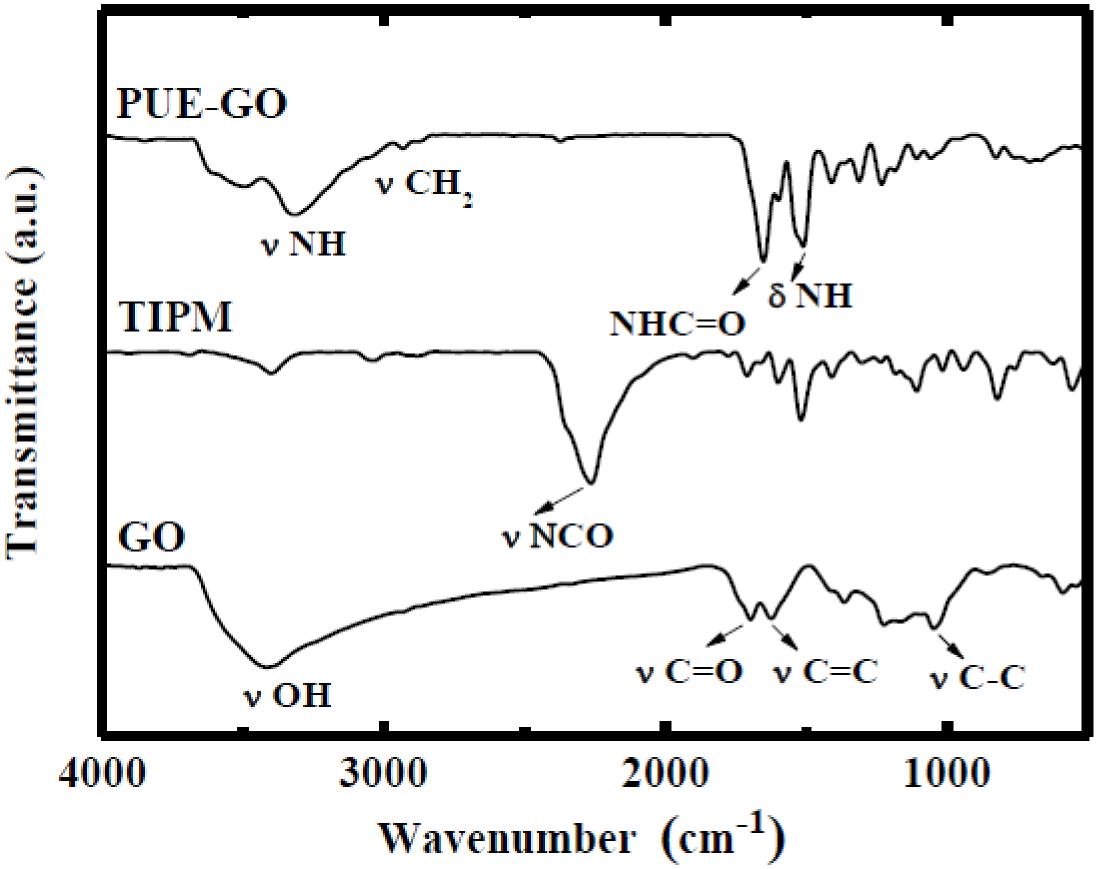

Figure 1: FTIR Spectra of (A) Tris(4-isocyanatophenyl)methane (TIPM), (B) Graphene Oxide (GO), (C) Poly(urethane-amide)- GO (PUE-GO) gel.

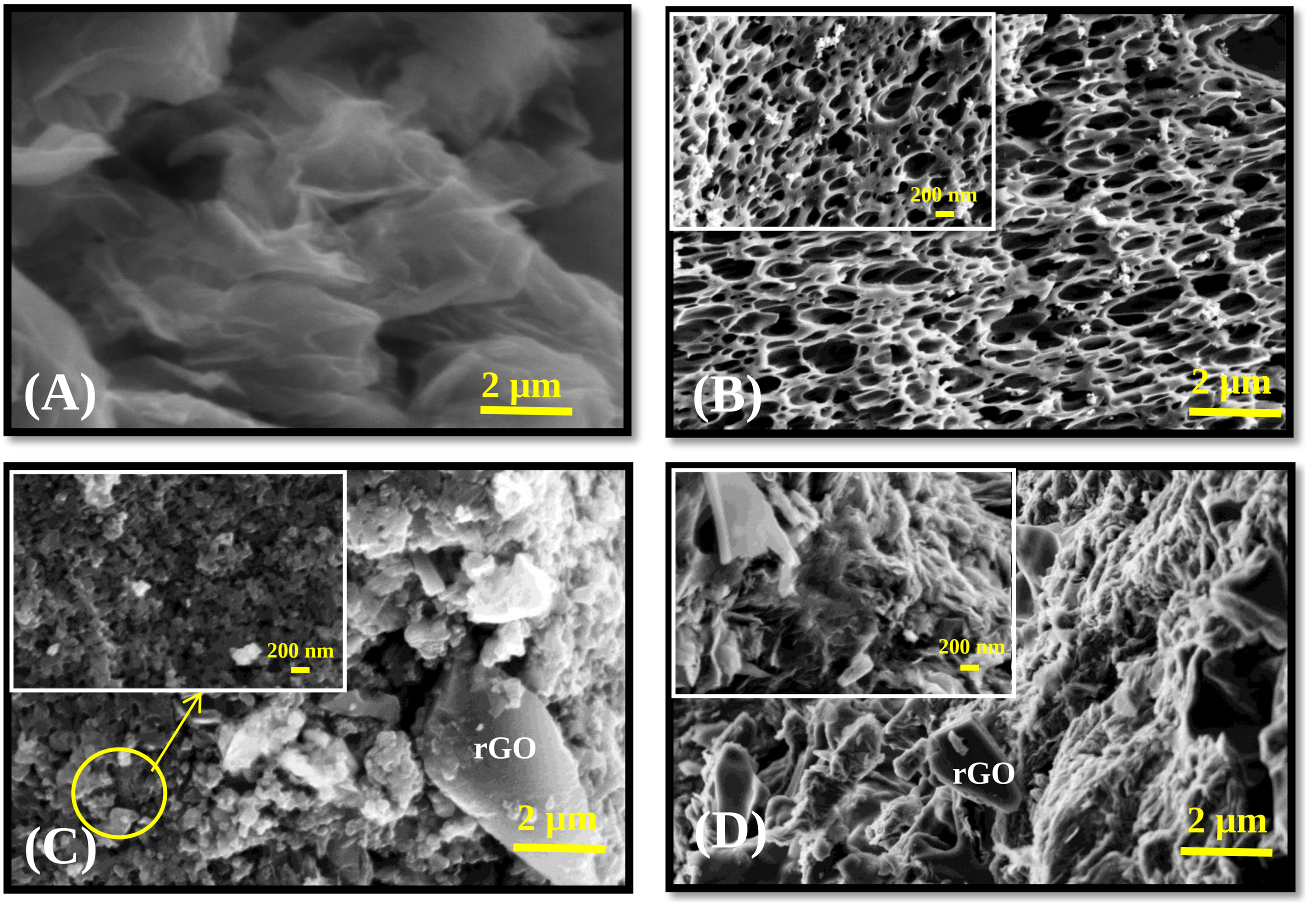

Figure 2: FE-SEM images of (A) Graphene Oxide (GO) (B) N-doped amorphous carbon aerogel (ACA) (C) N-doped amorphous carbon-rGO aerogel-2 (ACGA-2) (D) N-doped amorphous carbon-rGO aerogel-10 (ACGA-10).

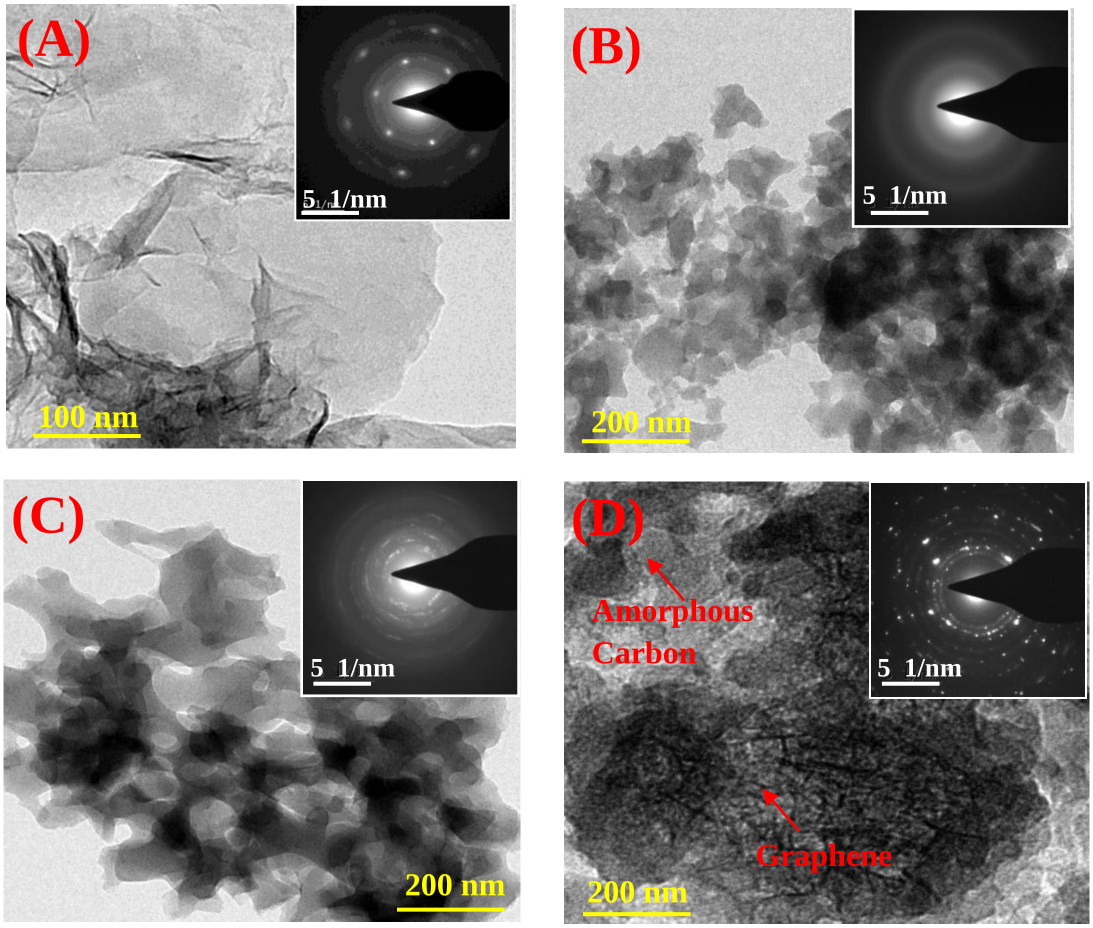

Figure 3: HR-TEM images of (A) Graphene Oxide (GO) (B) N-doped amorphous carbon aerogel (ACA) (C) N-doped amorphous carbon-rGO aerogel-2 (ACGA-2) (D) N-doped amorphous carbon-rGO aerogel-10 (ACGA-10). Inset: Selective Area Diffraction (SAED) Pattern of corresponding samples.

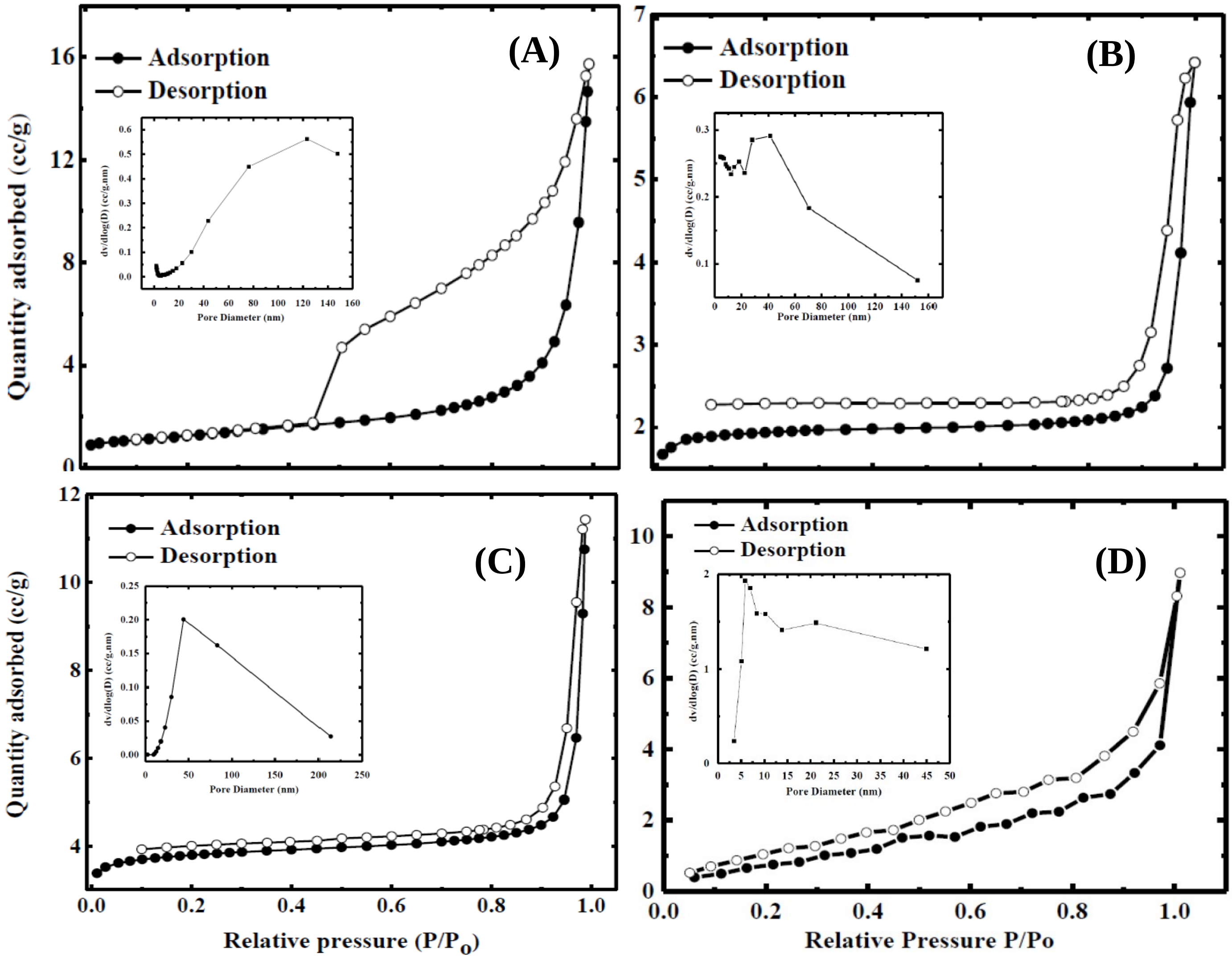

Figure 4. N_2 sorption isotherms of (A) Graphene Oxide (GO) (B) N-doped amorphous carbon aerogel (ACA) (C) N-doped amorphous carbon-rGO aerogel-2 (ACGA-2) (D) N-doped amorphous carbon-rGO aerogel-10 (ACGA-10). Inset: BJH pore size distribution plots for respective N_2 sorption isotherms

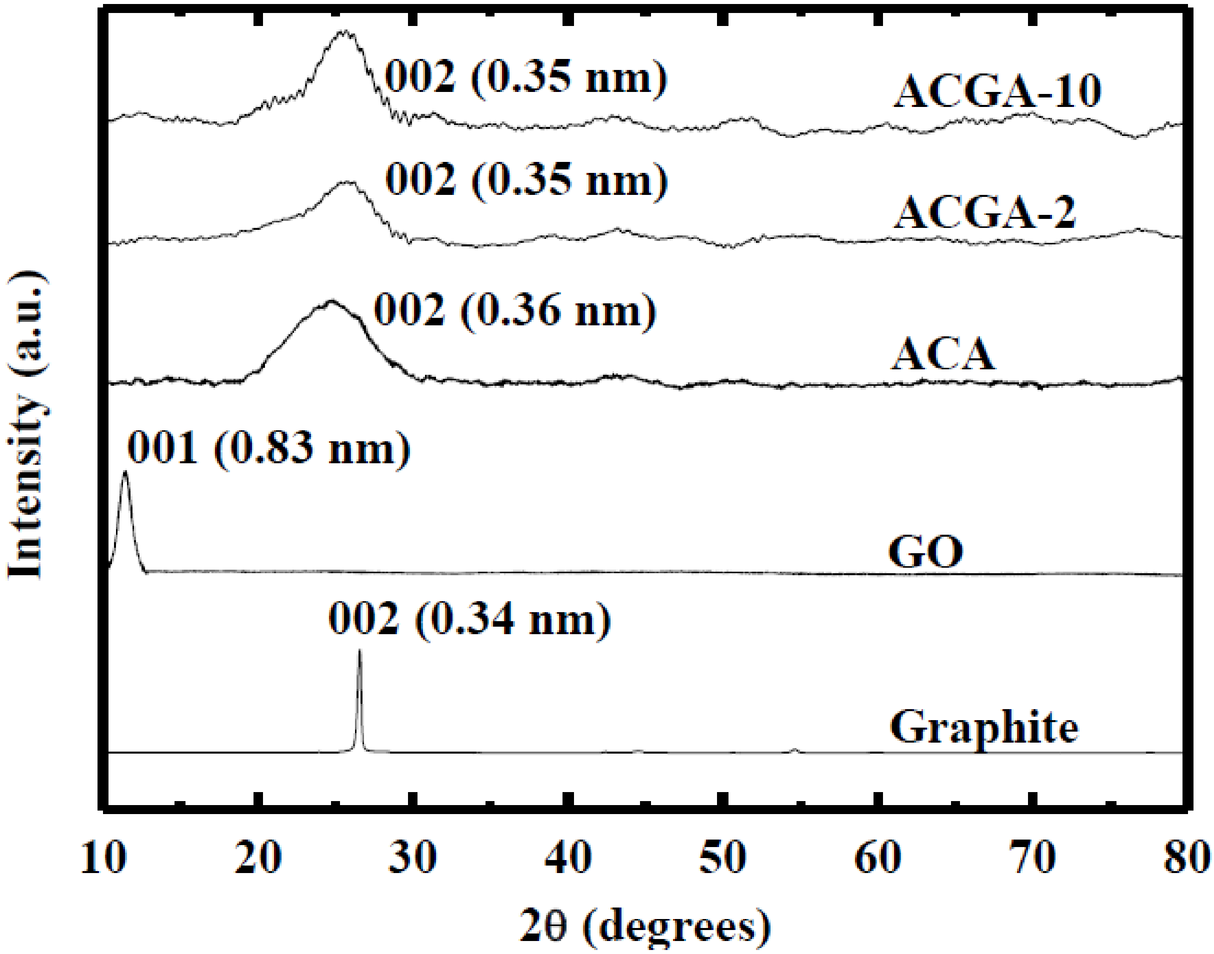

Figure 5. XRD of Graphite, Graphene Oxide (GO), N-doped amorphous carbon aerogel (ACA), N-doped amorphous carbon-rGO aerogel-2 (ACGA-2), N-doped amorphous carbon-rGO aerogel-10 (ACGA-10)

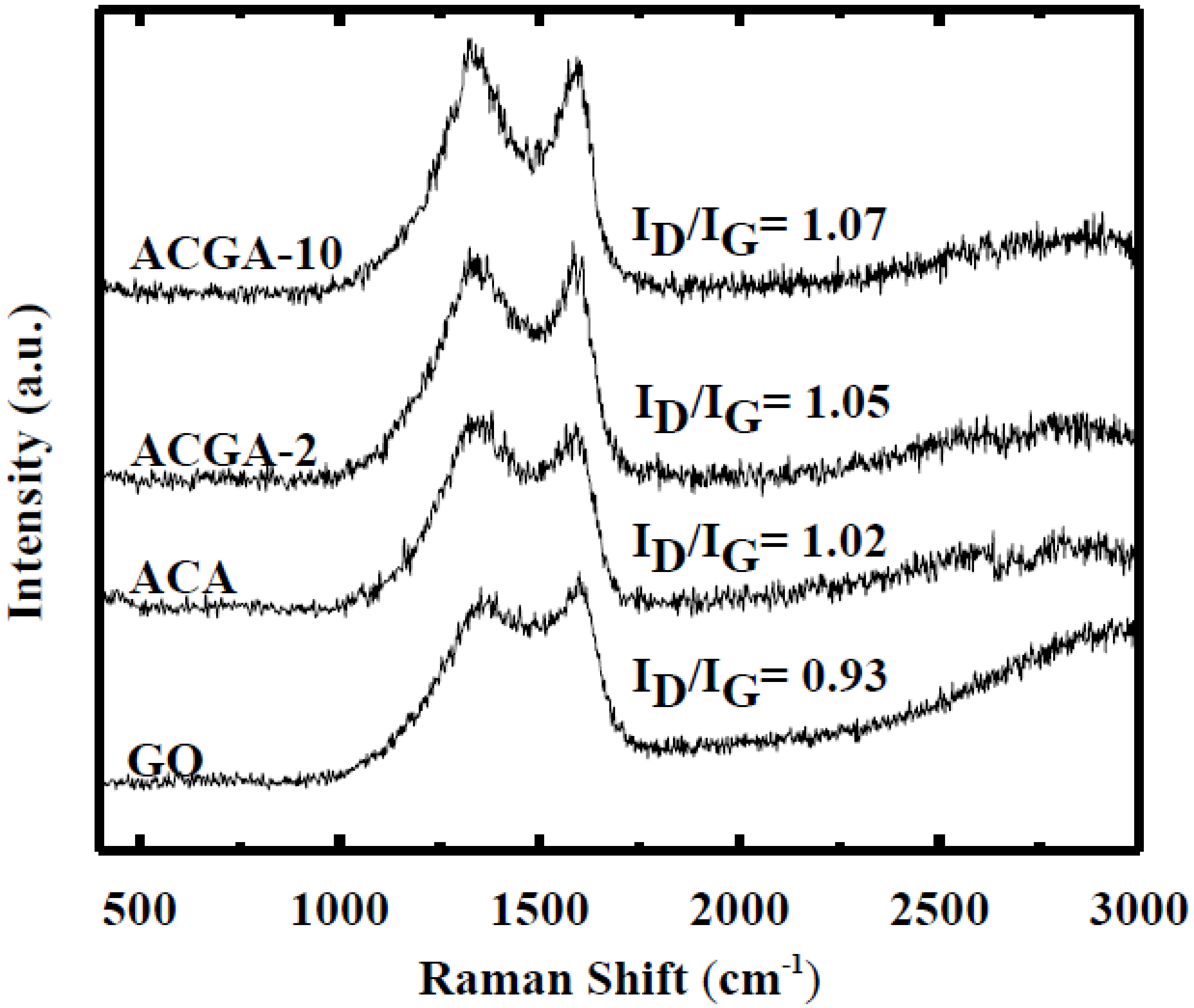

Figure 6. Raman Spectra of Graphene Oxide (GO), N-doped amorphous carbon aerogel (ACA), N-doped amorphous carbon-rGO aerogel-2 (ACGA-2), N-doped amorphous carbon-rGO aerogel-10 (ACGA-10).

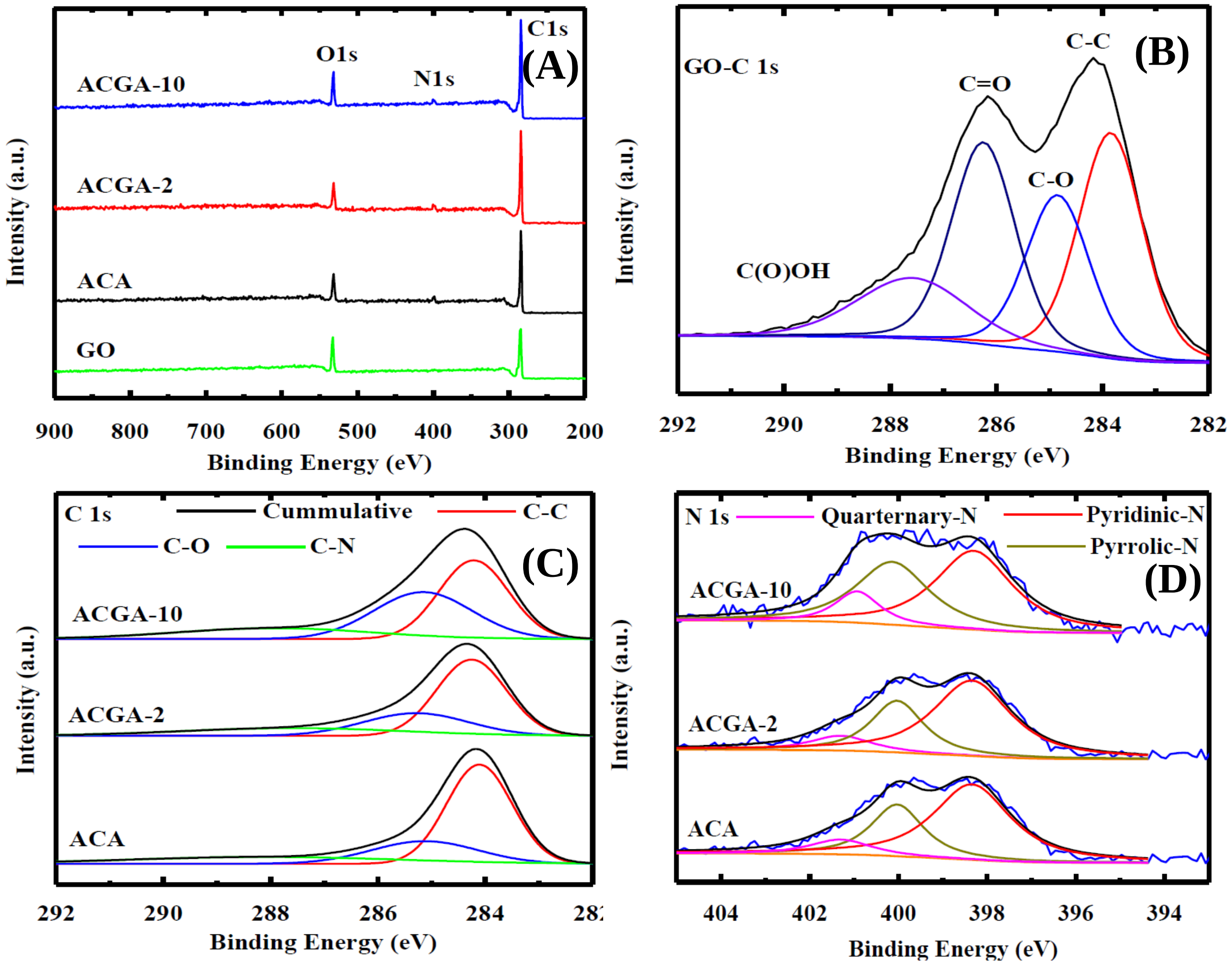

Figure 7. (A) XPS spectra of Graphene Oxide (GO), N-doped amorphous carbon aerogel (ACA), N-doped amorphous carbon-rGO aerogel-2 (ACGA-2), N-doped amorphous carbon-rGO aerogel-10 (ACGA-10), (B) C 1s spectra of Graphene Oxide (GO), (C) C 1s spectra of N-doped amorphous carbon aerogel (ACA), N-doped amorphous carbon-rGO aerogel-2 (ACGA-2), N-doped amorphous carbon-rGO aerogel-10 (ACGA-10), (D) N 1s spectra of N-doped amorphous carbon aerogel (ACA), N-doped amorphous carbon-rGO aerogel-2 (ACGA-2), N-doped amorphous carbon-rGO aerogel-10 (ACGA-10).

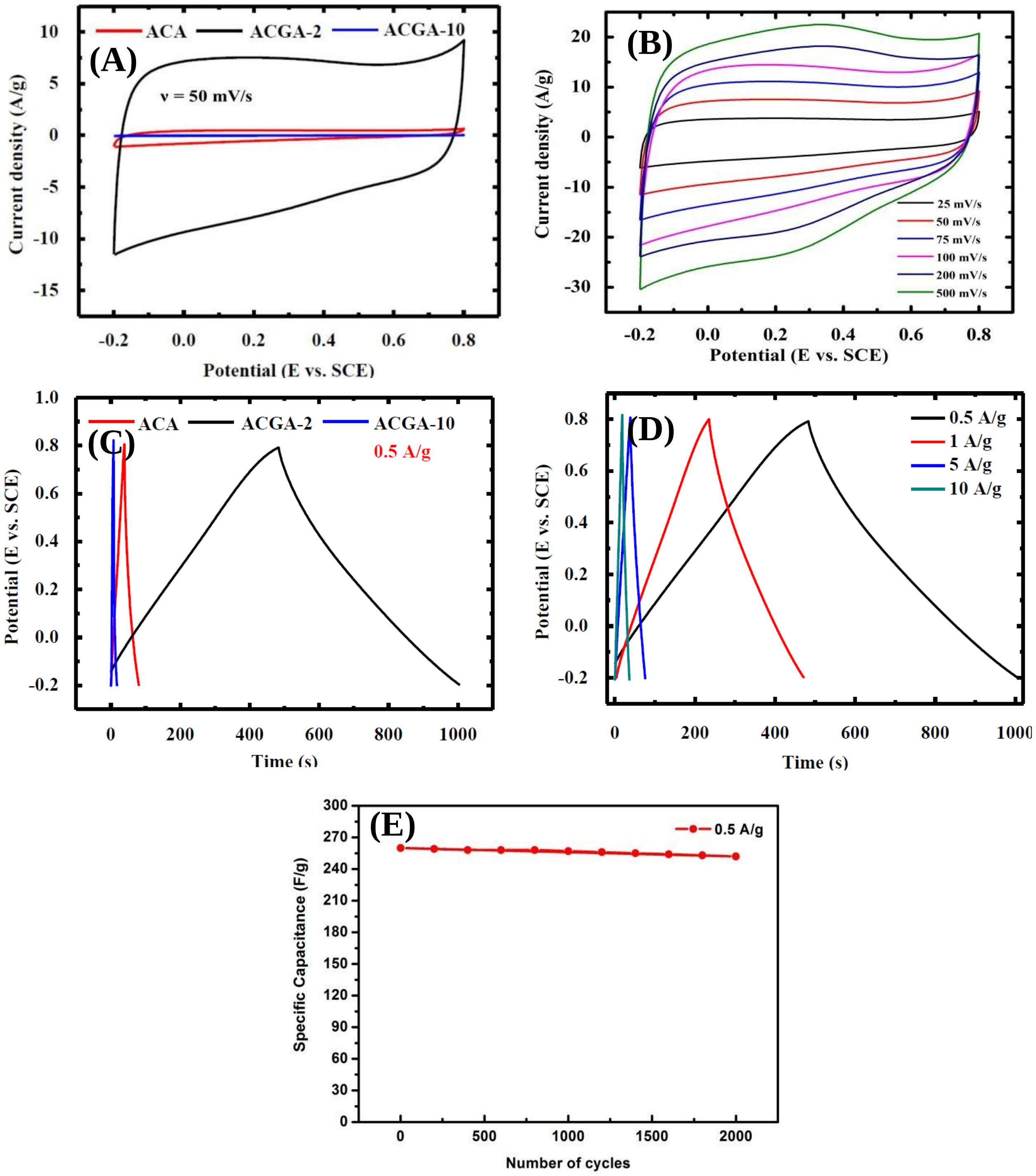

Figure 8:(A) Cyclic Voltammograms of N-doped amorphous carbon aerogel (ACA);N-doped amorphous carbon-rGO aerogel-2 (ACGA-2) and N-doped amorphous carbon-rGO aerogel-10 (ACGA-10) in 1 M H_2SO_4 at a scan rate of 50 mV/s; ;(B) Cyclic Voltammograms of ACGA-2 in 1 M H_2SO_4 at different scan rates; (C) Charge-discharge curve of ACA, ACGA-2 and ACGA-10 at a current density of 0.5 A/g in 1M H_2SO_4 ; (D) Charge-discharge curve of ACGA-2 at different current densities in 1 M H_2SO_4; (D) Electrochemical cycling stability of ACGA-2 after 2000 cycles at a current density of 0.5 A/g in 1 M H_2SO_4.

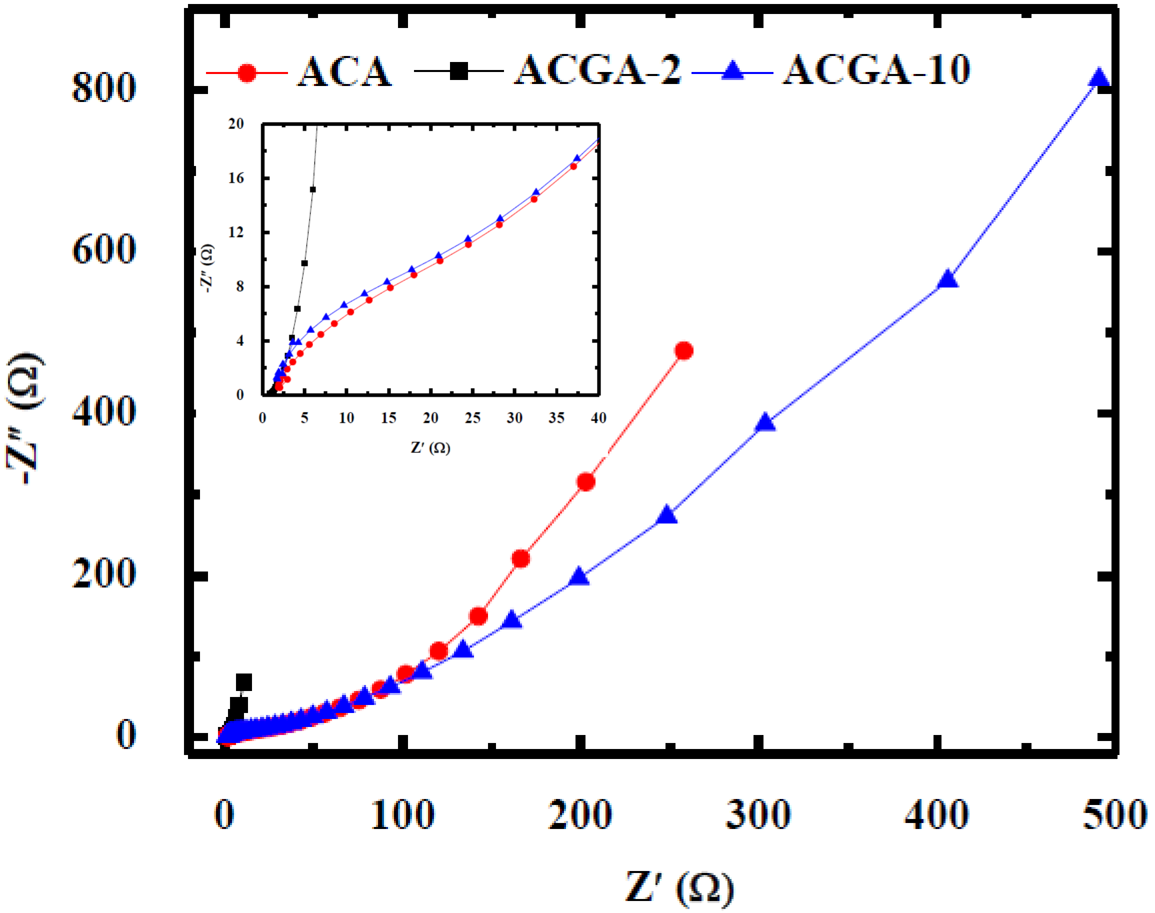

Figure 9. Nyquist plot of N-doped amorphous carbon aerogel (ACA), N-doped amorphous carbon-rGO aerogel-2 (ACGA-2), N-doped amorphous carbon-rGO aerogel-10 (ACGA-10)

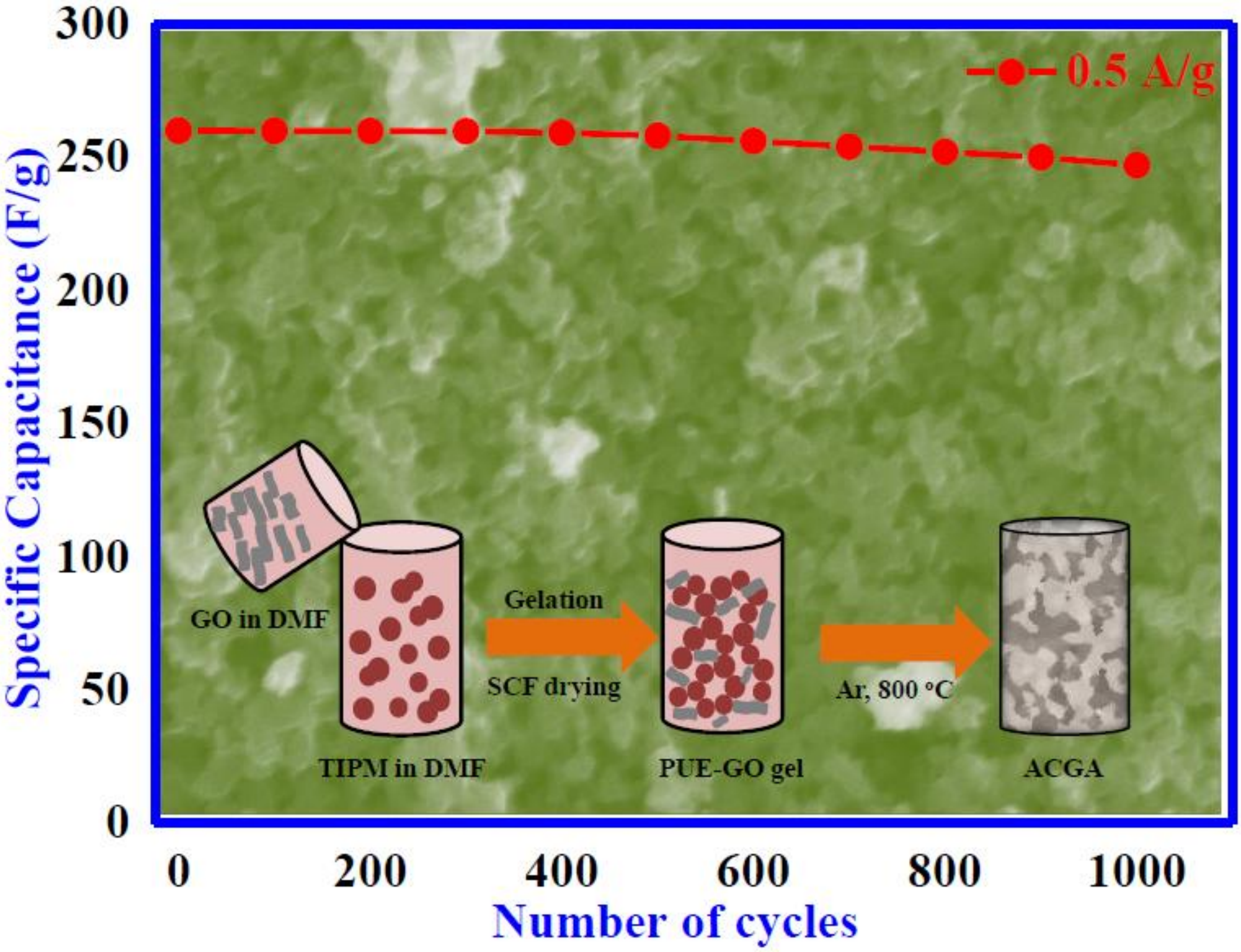
300
250
200
150
100
50
0
Specific Capacitance (F/g)
0
200
400
600
800
1000
Number of cycles
0.5 A/g
GO in DMF
TIPM in DMF
Gelation
SCF drying
PUE-GO gel
Ar, 800 °C
ACGA